Coordinate space Hartree-Fock-Bogoliubov calculations for the zirconium isotope chain up to the two-neutron drip line

A. Blazkiewicz, V. E. Oberacker, and A. S. Umar
Department of Physics and Astronomy, Vanderbilt University, Nashville, Tennessee 37235, USA

M. Stoitsov
Department of Physics and Astronomy, University of Tennessee, Knoxville, Tennessee 37996, USA
Physics Division, Oak Ridge National Laboratory, P.O. Box 2008, Oak Ridge, Tennessee 37831, USA
Joint Institute for Heavy-Ion Research, Oak Ridge, Tennessee 37831, USA
Institute of Nuclear Research and Nuclear Energy, Bulgarian Academy of Science, Sofia BG-1784, Bulgaria
(Received 21 February 2005; published 31 May 2005)

We solve the Hartree-Fock-Bogoliubov (HFB) equations for deformed, axially symmetric even-even nuclei in coordinate space on a two-dimensional (2-D) lattice utilizing the basis-spline expansion method. Results are presented for the neutron-rich zirconium isotopes up to the two-neutron drip line. In particular, we calculate binding energies, two-neutron separation energies, normal and pairing densities, mean square radii, quadrupole moments, and pairing gaps. Very large prolate quadrupole deformations ($\beta_2 = 0.42, 0.43, 0.47$) are found for the ^{102,104,112}Zr isotopes, in agreement with recent experimental data. We compare 2-D basis-spline lattice results with the results from a 2-D HFB code that uses a transformed harmonic oscillator basis.

DOI: 10.1103/PhysRevC.71.054321 PACS number(s): 21.60.Jz

I. INTRODUCTION

In contrast to the well-understood behavior near the valley of stability, there are many open questions as we move toward the neutron drip line. In this exotic region of the nuclear chart, one expects to see several new phenomena [1]: the neutron-matter distribution is very diffuse giving rise to the "neutron skins" and the "neutron halos". One also expects new collective modes associated with the neutron skin, e.g., the "scissors" vibrational mode [2].

In current experiments, the neutron drip line has only been reached for relatively light nuclei. The second-generation radioactive ion beam facilities currently under construction will allow us to explore nuclear structure and astrophysics at the drip lines of heavier nuclei.

It is generally acknowledged that an accurate theoretical treatment of the pairing interaction is essential for a description of the exotic nuclei [3,4]. Besides large pairing correlations, the Hartree-Fock-Bogoliubov (HFB) calculations have to face the problem of an accurate description of the continuum states with a large spatial extent. All of these features represent major challenges for the numerical solution.

There are various mean-field methods for solving the nonrelativistic HFB equations. Generally, they can be divided into two categories: lattice methods and basis expansion methods. In the lattice approach, no region of the spatial lattice is favored over any other region: the well-bound, weakly bound, and (discretized) continuum states can be represented with the same accuracy. Among the codes that solve the HFB problem on a lattice in coordinate space using the quasiparticles we have one-dimensional a (1-D) (spherical) HFB code [5] and the present two-dimensional (2-D) (axially symmetric) code [3,4,6]. In the basis expansion method, a wave function is expanded into the chosen basis functions: the harmonic oscillator basis (HO) [7] or the transformed harmonic oscillator basis (THO) [8]. The HFB equations have also been solved in coordinate space by means of the two-basis method [9] where one uses a truncated basis composed of bound and discretized continuum states up to a few MeV in the continuum [10]. In an alternative approach, the HFB equations are solved on a three-dimensional (3-D) Cartesian mesh using the canonical-basis approach [11].

We solve the HFB equations for deformed, axially symmetric nuclei in coordinate space on a 2-D lattice [3,4]. Our computational technique (the basis-spline collocation and Galerkin method) is particularly well suited to studying the ground state properties of nuclei near the drip lines. It allows us to take into account high-energy continuum states up to an equivalent single-particle energy of 60 MeV or more.

In this paper, we study the ground state properties of neutron-rich zirconium nuclei ($Z = 40$) up to the two-neutron drip line. The isotope chain calculations start from the ^{102}Zr isotope up to the drip-line nucleus, which turns out to be ^{122}Zr. For a long time, the $A \sim 100$ region has been of interest to nuclear structure physicists as an area of competition between various coexisting nuclear shapes (well-deformed prolate, oblate, or spherical) [12]. The zirconium isotopes are known to possess a rapidly changing nuclear shape when the neutron number changes from 56 to 60 [13]. We find that a spherical ground state shape is preferred over a prolate shape starting from the ^{114}Zr isotope up to the drip-line nucleus ^{122}Zr. In this paper, we compare basis-spline lattice results with the HFB-2D-THO code [8], as well as with currently available experimental data.

II. SKYRME-HFB EQUATIONS IN COORDINATE SPACE

A detailed description of the basis-spline lattice method has been published in references [3,4]; we give here only a

brief summary. In coordinate space representation, the HFB Hamiltonian and the quasiparticle wave functions depend on the distance vector $\mathbf{r}$, spin projection $\sigma = \pm\frac{1}{2}$, and isospin projection $q = \pm\frac{1}{2}$ (corresponding to protons and neutrons, respectively). In the HFB formalism, there are two types of quasiparticle (bi-spinor) wave functions, ϕ_1 and ϕ_2. In the present work, we utilize a Skyrme effective N-N interaction in the particle-hole channel while the p-p and h-h channels are described by a zero-range Δ pairing force. For these types of effective interactions, the particle mean-field Hamiltonian h and the pairing field Hamiltonian $\tilde{h}$ are diagonal in isospin space and local in position space, and the HFB equations have the following structure [3]:

$$\begin{bmatrix} (h^q - \lambda) & \tilde{h}^q \\ \tilde{h}^q & -(h^q - \lambda) \end{bmatrix} \begin{pmatrix} \phi^q_{1,\alpha} \\ \phi^q_{2,\alpha} \end{pmatrix} = E^q_\alpha \begin{pmatrix} \phi^q_{1,\alpha} \\ \phi^q_{2,\alpha} \end{pmatrix}, \tag{1}$$

where the Lagrange parameter λ is introduced to yield the correct particle number on average since the HFB wave function does not have a well-defined particle number.

The quasiparticle energy spectrum is discrete for $|E| < -\lambda$ and continuous for $|E| > -\lambda$ [5]. For even-even nuclei, it is customary to solve the HFB equations for positive quasiparticle energies and consider all negative energy states as occupied in the HFB ground state. The quasiparticle wave functions determine the normal density $\rho_q(\mathbf{r})$ and the pairing density $\tilde{\rho}_q(\mathbf{r})$ as follows

$$\rho_q(\mathbf{r}) = \sum_{E_\alpha>0}^{\infty} \sum_{\sigma=-\frac{1}{2}}^{+\frac{1}{2}} \phi^q_{2,\alpha}(\mathbf{r}\sigma)\phi^{q*}_{2,\alpha}(\mathbf{r}\sigma), \tag{2}$$

$$\tilde{\rho}_q(\mathbf{r}) = -\sum_{E_\alpha>0}^{\infty} \sum_{\sigma=-\frac{1}{2}}^{+\frac{1}{2}} \phi^q_{2,\alpha}(\mathbf{r}\sigma)\phi^{q*}_{1,\alpha}(\mathbf{r}\sigma). \tag{3}$$

Restricting ourselves to axially symmetric nuclei, we use cylindrical coordinates (r, z, ϕ). In the HFB lattice method, we introduce a 2-D grid (r_α, z_β) with $\alpha = 1, \ldots, N_r$ and $\beta = 1, \ldots, N_z$. In radial direction, the grid spans the region from 0 to $r_{\max}$. Because we want to be able to treat octupole shapes, we do not assume left-right symmetry in z direction. Consequently, the grid extends from $-z_{\max}$ to $+z_{\max}$. Typically, $z_{\max} \approx r_{\max}$ and $N_z \approx 2 \cdot N_r$. The HFB wave functions and operators are represented on the 2-D lattice by basis-spline expansion techniques. In practice, basis splines of order $M = 9$ are being used. Details about the basis-spline collocation and Galerkin methods are given in the Appendix.

III. NUMERICAL RESULTS AND COMPARISON WITH EXPERIMENTAL DATA

This section describes the numerical results for the even-even members of the zirconium ($Z = 40$) isotope chain up to the two-neutron drip line. Two theoretical approaches are presented and compared: (a) a 2-D lattice method using basis-spline technology (hereafter referred to as HFB-2D-LATTICE) and (b) an expansion in a 2-D harmonic oscillator (HFB-2D-HO) and transformed harmonic oscillator basis (HFB-2D-THO). We also compare theoretical results with experimental data whenever possible. In all calculations, we utilize the SLy4 Skyrme force [14] and a zero-range pairing force with a strength parameter $V_0 = -187.1305$ (HFB-2D-LATTICE CODE), and $V_0 = -187.1000$ (HFB-2D-THO CODE) with an equivalent single-particle energy [3,15] cutoff parameter of $\varepsilon_{\max} = 60$ MeV. The pairing strength V_0 has been adjusted in both codes to reproduce the measured average neutron pairing gap of 1.245 MeV in ^{120}Sn [5], as can be seen from Table I.

TABLE I. Results for $^{120}_{50}$Sn. Comparison of results obtained from the HFB-2D-LATTICE code (first row) with HFB-2D-THO results (second row) and the experiment (third row). The columns display binding energies (BE), intrinsic quadrupole moments for neutrons and protons (Q_n,Q_p), rms radii (r_n,r_p), average pairing gaps (Δ_n, Δ_p), pairing energy for neutrons (PE_n), and Fermi levels (λ_n, λ_p).

BE(MeV)	Q_n(fm^2)	Q_p(fm^2)	r_n(fm)	r_p(fm)
−1019.26	0.29	0.12	4.725	4.590
−1018.22	0.00	0.00	4.728	4.593
−1020.54	–	–	–	–
Δ_n(MeV)	Δ_p(MeV)	PE_n(MeV)	λ_n(MeV)	λ_p(MeV)
1.244999	0.0	−10.24	−7.98	−8.16
1.245469	0.0	−10.26	−7.99	−11.13
1.245	–	–	–	–

In Table I we compare the results from the two HFB codes for the $^{120}_{50}$Sn isotope. All observables agree very well. The apparent "disagreement" in the proton Fermi level λ_p is really an artifact: the pairing gap vanishes at the magic proton number $Z = 50$ resulting in an ill-defined Fermi energy. The two codes use different prescriptions for calculating λ_p in the trivial case of no pairing. HFB+THO accepts the last occupied equivalent single-particle energy as λ_p in this no-pairing case, whereas the basis-spline code takes the average of the last occupied and first unoccupied equivalent single-particle energy levels.

A. Deformations, drip line, and pairing properties

Recently, triple-γ coincidence experiments carried out with the Gammasphere at LBNL [16] have determined half-lives and quadrupole deformations of the neutron-rich ^{102,104}Zr isotopes. The isotopes from that region are produced in the process of fission of transuranic elements and have been studied via γ-ray spectroscopy techniques. These medium-mass nuclei are among the most neutron-rich isotopes ($N/Z \approx 1.6$) for which spectroscopic data are available. Very large prolate quadrupole deformations ($\beta_2 = 0.43, 0.45$) are found for the ^{102,104}Zr isotopes. Furthermore, the laser spectroscopy measurements [12] for the zirconium isotopes have yielded precise rms radii in this region. Recently, an experiment was carried out to measure the mass of the ^{104}Zr isotope [13]. It is therefore of great interest to compare these data with the predictions of the self-consistent HFB mean-field theory.

In radial r direction, the lattice in the HFB-2D-LATTICE code extends from 0 to −15 fm; and in symmetry axis z direction, from −15 to +15 fm, with a lattice spacing of about 0.8 fm in the central region. Angular momentum projections $\Omega = 1/2, 3/2, \ldots, 21/2$ were taken into account.

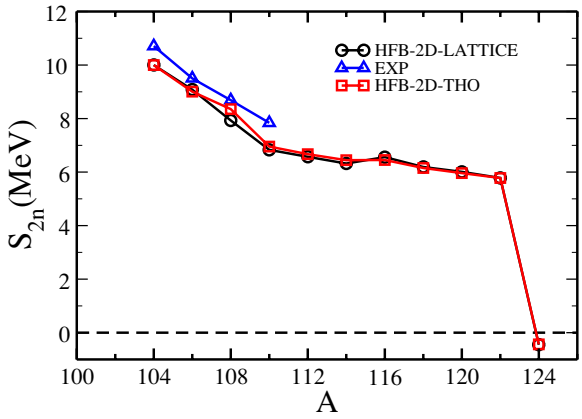

FIG. 1. (Color online) Two-neutron separation energies for the neutron-rich zirconium isotopes. The drip line is located where the separation energy becomes zero. The ^{122}Zr isotope is the last stable nucleus against two-neutron emission.

Calculations performed with the HFB-2D-THO code used 20 transformed harmonic oscillator shells. Figure 1 shows the calculated two-neutron separation energies for the zirconium isotope chain. The two-neutron separation energy is defined as

$$S_{2n}(Z, N) = E_{\text{bind}}(Z, N) - E_{\text{bind}}(Z, N-2). \qquad (4)$$

Note that in using this equation, all binding energies must be entered with a *positive* sign. The position of the two-neutron drip line is defined by the condition $S_{2n}(Z, N) = 0$, and nuclei with negative two-neutron separation energy are unstable against the emission of two neutrons. As one can see, both methods (HFB-2D-THO and HFB-2D-LATTICE) are in excellent agreement for the two-neutron separation energy for the entire isotope chain. Particularly, the ^{122}Zr isotope is predicted in both calculations as the drip-line nucleus. In addition, we also give a comparison with the latest experimental data, available only up to the isotope ^{110}Zr [17]. As shown on Fig. 1, the separation energy values obtained from the experiment are somewhat larger than the theoretical calculations although the trend remains the same.

In Fig. 2, we compare the intrinsic proton and neutron quadrupole moments calculated with the LATTICE code and

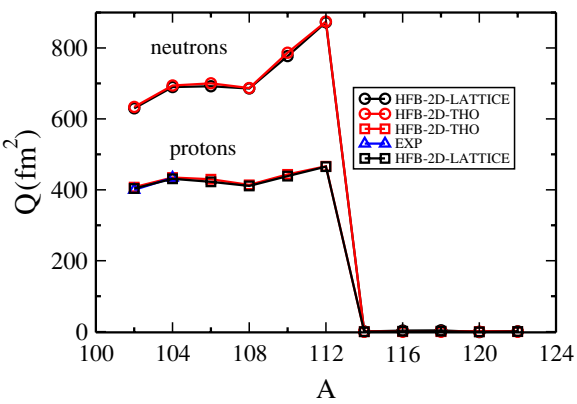

FIG. 2. (Color online) Intrinsic quadrupole moments for protons and neutrons.

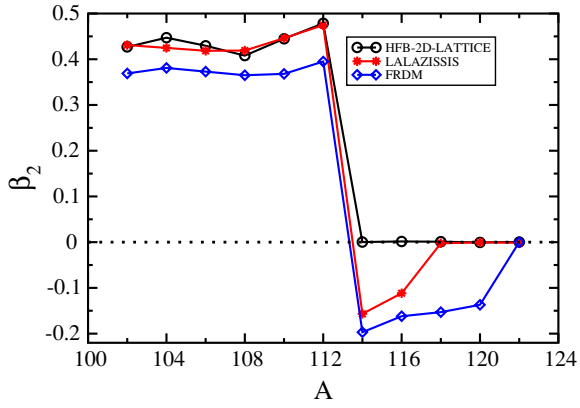

FIG. 3. (Color online) Mass quadrupole parameter β_2 comparison for neutrons. Calculations by Lalazissis *et al*. [19], HFB-2D-LATTICE, and Möller *et al*. [18] (FRDM) (β_2 total is shown).

the THO code. Available experimental data [16] are also given. Generally, we observe a nearly perfect agreement between the two codes as well as with the experiment. The deformations (for neutrons) in terms of the deformation parameter β_2 for those nuclei, namely, for the $^{102-112}$Zr isotopes range from $\beta_2 = 0.42$ to $\beta_2 = 0.47$. Both the basis-spline lattice code and the HFB-2D-THO code predict the ^{112}Zr isotope to have the largest ground state deformation. For mass numbers larger than 112, we observe a transition to spherical ground state shape. This phenomenon had been also found in calculations performed by Möller *et al*. [18] [finite range droplet model calculations (FRDM)] and in relativistic mean-field calculations by Lalazissis *et al*. [19]. We depict this comparison in Fig. 3 . Experimental deformations for protons are available for two isotopes, ^{102}Zr and ^{104}Zr [16]. Calculations agree with the experiment reasonably well and give β_2 values of 0.42, 0.43; while the experiment predicts $\beta_2^{102} = 0.42$, $\beta_2^{104} = 0.45$.

In Fig. 4, we compare the root-mean-square radii of protons and neutrons predicted by the LATTICE code and the THO code. Both codes give nearly identical results for the whole isotope chain. Only one experimental data point is available, the proton rms radius of ^{102}Zr [12]. The experiment yields a

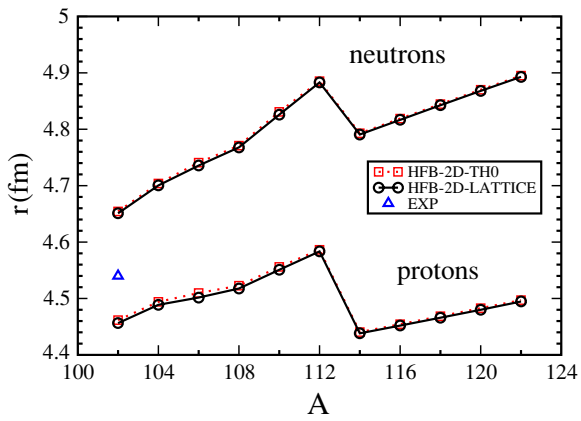

FIG. 4. (Color online) Root-mean-square radii for the chain of zirconium isotopes.

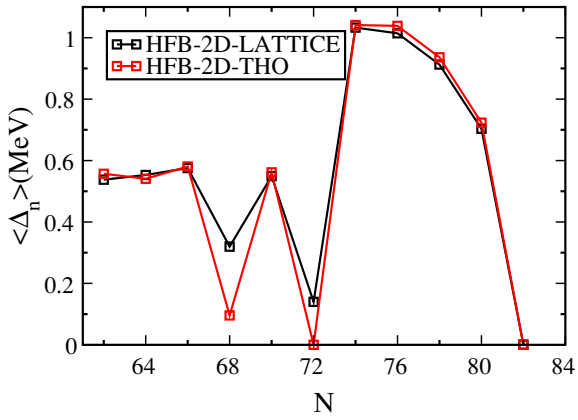

FIG. 5. (Color online) Average neutron pairing gap for the chain of zirconium isotopes.

proton rms radius of 4.54 fm while the HFB codes predict a value of 4.45 fm (HFB-2D-LATTICE) and 4.46 fm (HFB-2D-THO). The difference between theory and experiment is quite small, about 2%. We can clearly observe the presence of the neutron skin manifested by the large differences between the neutron and proton rms radii for all of the isotopes in the chain. As expected, the neutron skin becomes "thicker" as we approach the drip line. Starting at the mass number $A = 114$ and up to the drip line, the nuclei prefer a spherical ground state shape (Fig. 2), which results in a sudden shrinking of the rms radius at $A = 114$. Figures 5 and 6 depict the average pairing gaps for neutrons and protons. Generally, both HFB codes show the same trend for the pairing gaps as a function of neutron number; the agreement is noticeably better for neutrons. The two HFB codes predict a small value of the neutron pairing gap for the ^{112}Zr isotope which on the other hand has the largest prolate deformation (Fig. 2) among the calculated nuclei. Coincidentally, the drip line turns out to be at the neutron magic number ($N = 82$) and, as expected, both codes yield a pairing gap of zero for the ^{122}Zr isotope. The differences observed in the neutron and proton pairing gaps can be attributed to different approaches in representing the continuum states, namely discretized continuum states in the HFB-2D-LATTICE versus positive energy bound states in a

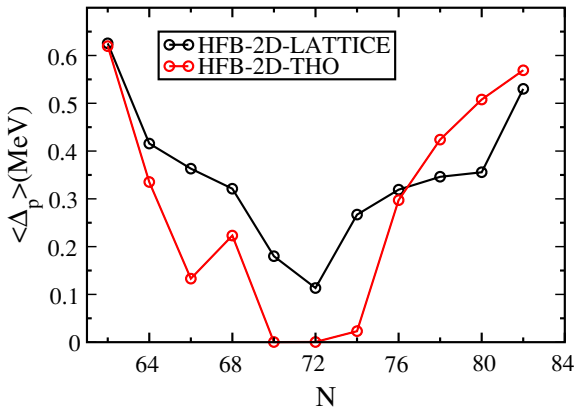

FIG. 6. (Color online) Average proton pairing gap for the chain of zirconium isotopes.

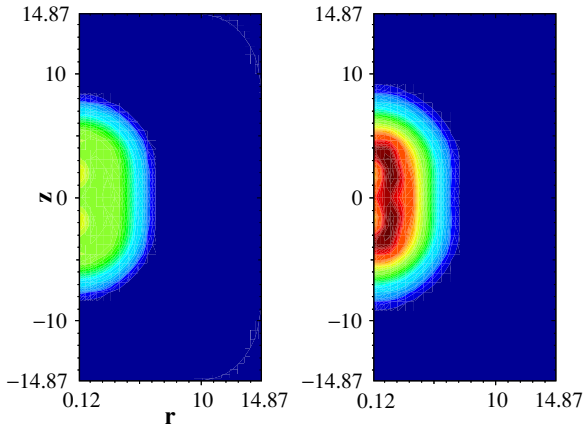

FIG. 7. (Color online) Contour plots of the ^{110}Zr normal densities, for protons (left) and neutrons (right). Densities are shown as a function of the cylindrical coordinates (r, z), where z is the symmetry axis. The scale ranges from 9.7×10^{-2} fm^{-3} (dark red), through 5.0×10^{-2} (light green), 3.0×10^{-3} (light blue), to 3.4×10^{-15} (dark blue).

stretched harmonic oscillator. In general, the pairing gap is the one observable that is most sensitive to the properties of the continuum states. In addition, two approaches use different methods for representing differential operators as well as calculating the Coulomb potential.

B. Density studies

In this section, we focus on the normal and pairing densities for the selected isotopes. In Fig. 7, we show a contour plot of normal densities for protons and neutrons for the ^{110}Zr isotope. It is the last deformed isotope with a significant value of the pairing gap for neutrons (Fig. 5); therefore, it is possible to show plots of both normal and pairing densities. The results obtained for the neutron normal and pairing densities (Figs. 7 and 8) clearly exhibit a large prolate deformation. The normal density for neutrons (Fig. 7) is concentrated in the region that extends from 0 to 2 fm in the r direction and from -5 to $+5$ fm in the z direction. Within this region, we find an enhancement in the neutron density with a shape that resembles the figure "eight." In comparing the neutron and proton densities, one notices that in the former, both the center of the nucleus and the surface is dominated by neutrons. The pairing density for neutrons in Fig. 8 shows a richer structure than the normal density. This quantity describes the probability of correlated nucleon pair formation with opposite spin projection, and it determines the pair transfer form factor. We can see that most correlated pair formation takes place in the four closed shaped structured areas near the z axis. We may conclude that neutrons dominate the pairing properties of this nucleus, which is a consequence of Δ_n being larger than Δ_p. A similar argument applies to normal densities ($N > Z$), yet the difference between neutrons and protons is more pronounced in the case of the pairing densities. A graph depicting the single-particle energy spectrum of the pairing density for the ^{104}Zr isotope has been published in Ref. [6]. In Figs. 9 and 10,

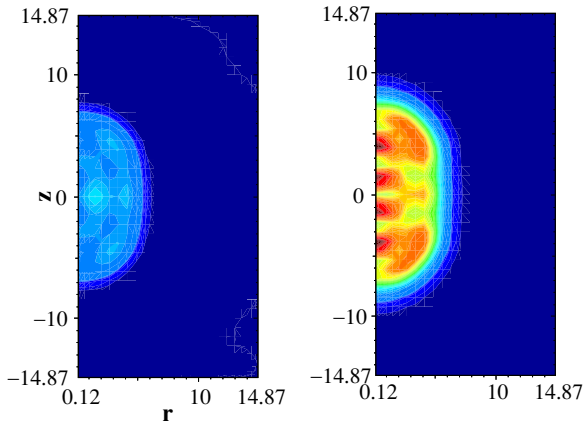

FIG. 8. (Color online) Contour plots of the ^{110}Zr pairing densities, for protons (left) and neutrons (right). The densities are shown as a function of the cylindrical coordinates (r, z), where z is the symmetry axis. The scale ranges from 9.0×10^{-3} fm^{-3} (dark red), through 4.9×10^{-3} (light green), 8.0×10^{-4} (light blue), to 9.3×10^{-14} (dark blue).

we show plots of normal densities as a function of the distance from the center, $r = \sqrt{\rho^2 + z^2}$. For a given value of r, the density is single-valued for a spherical nucleus and multi-valued for a deformed density distribution because in the latter case different combinations of lattice points z_i and ρ_j give rise to the same r-value. In Fig. 9 we compare three different calculations of the neutron normal density for the most deformed ^{112}Zr isotope. The plot on a logarithmic scale shows that the density distribution predicted by the HFB-2D-THO and HFB-2D-LATTICE codes is deformed for almost all values of the distance from the nuclear center r. At very large distances, the densities become less deformed since nuclear potentials go to zero and HFB equations lead to a spherical asymptotic solution. Figure 9 also shows for comparison the HFB-2D-HO result as an illustration of the shortcomings of the pure harmonic oscillator basis calculations to reproduce density distributions asymptoticlally at very large distances.

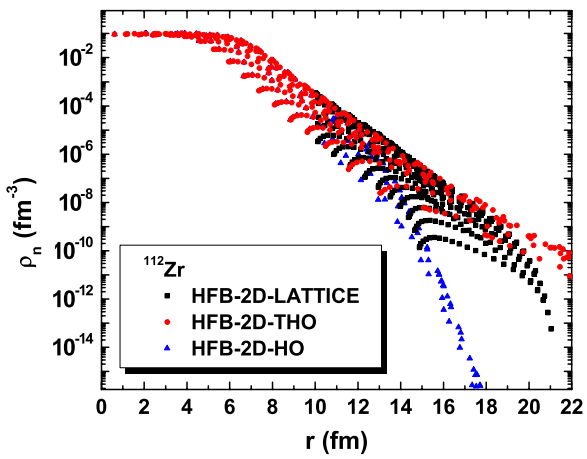

FIG. 9. (Color online) Logarithmic plot of the normal neutron density for the most deformed isotope ^{112}Zr as a function of the distance $r = \sqrt{\rho^2 + z^2}$.

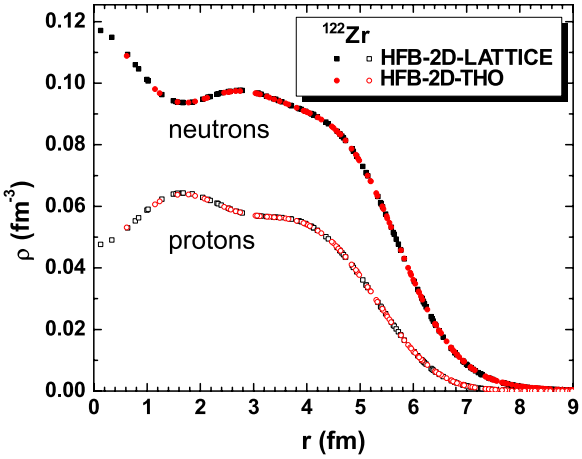

FIG. 10. (Color online) Linear plots of the normal neutron and proton densities for the drip line nucleus ^{122}Zr as a function of distance $r = \sqrt{\rho^2 + z^2}$. Comparison between the HFB-2D-THO code and the HFB-2D-LATTICE code.

One can see its too rapid decay beyond distances of about 12 fm. Clearly, the pure harmonic oscillator basis calculations cannot represent properly the density asymptotic for nuclei close to the neutron drip line. Neutron and proton normal densities for the drip-line nucleus ^{122}Zr are shown in Fig. 10. From the single-valued plot as a function of $r = \sqrt{\rho^2 + z^2}$, one can immediately conclude that both neutron and proton normal densities are spherical. Another feature is the strong neutron enhancement at the center and a corresponding depletion in the proton density, which is due to occupied (unoccupied) s orbitals near the Fermi level. We also note that the neutron density is substantially larger than the proton density for all values of r.

IV. CONCLUSIONS

In this paper, we performed Skyrme-HFB calculations in coordinate space for the neutron-rich zirconium isotopes up to the two-neutron drip line. We calculated the ground state properties (even-even nuclei) for the zirconium isotopes ($Z = 40$), starting from $N = 62$ up to the two-neutron drip line, which our HFB codes predict to be $N = 82$. In particular, we calculated the two-neutron separation energies, quadrupole moments, rms radii, average pairing gaps, and densities. In comparing HFB-2D-LATTICE theoretical calculations for the two-neutron separation energies (Fig. 1) with the HFB-2D-THO code, we find the same results. Particularly, both codes predict the ^{122}Zr isotope to be the drip line nucleus. We find very large prolate deformations for the $^{102-112}$Zr isotopes and a spherical ground state shape for the $^{114-122}$Zr nuclei. The β_2 value for the most deformed nucleus ^{112}Zr in the calculated chain reaches an impressive value of 0.47. The root-mean-square radii clearly show the existence of a "neutron skin" in the neutron-rich zirconium isotopes. We can also observe a sudden shrinking of the rms radius at $A = 114$ due to a change of the prolate ground state deformation into the spherical shape. In Sec. III B, we studied normal and pairing densities. In particular, Figs. 7 and 8 show that for $N > Z$ and $\Delta_n > \Delta_p$ both normal and pairing densities are dominated by neutrons. The density

studies in Fig. 10 predict the presence of a sizable neutron skin in the spherical drip line nucleus ^{122}Zr.

ACKNOWLEDGMENTS

This work has been supported by the U.S. Department of Energy under Grant No. DE-FG02-96ER40963 with Vanderbilt University, by the U.S. Department of Energy under Contract Nos. DE-FA02-96ER40963 (University of Tennessee), DE-AC05-00OR22725 with UT-Battelle, LLC (Oak Ridge National Laboratory), and DE-FG05-87ER40361 (Joint Institute for Heavy Ion Research), The National Science Foundation Contract No. 0124053 (U.S.-Japan Cooperative Science Award); and by the National Nuclear Security Administration under the Stewardship Science Academic Alliances program through DOE Research Grant DE-FG03-03NA00083. Some of the numerical calculations were carried out at the IBM-RS/6000 SP supercomputer of the National Energy Research Scientific Computing Center which is supported by the Office of Science of the U.S. Department of Energy. Additional computations were performed at Vanderbilt University's ACCRE multiprocessor platform.

APPENDIX: BASIS-SPLINE REPRESENTATION OF WAVE FUNCTIONS AND OPERATORS

In this Appendix, we discuss the representation of differential operators and wave functions in terms of basis splines which are used in the HFB-2D-LATTICE code. There exists an extensive literature on basis-spline theory developed by mathematicians [20]. We have adapted some of these methods for the numerical solution of problems in atomic and nuclear physics on a lattice. Reference [21] discusses the basis-spline collocation method, periodic and fixed boundary conditions, and the solution of various 1-D radial problems (Schrödinger, Poisson, and Helmholtz equations) and the solution of 3-D Cartesian problems (Poisson equation). In a later paper, Umar *et al*. [22] solved the HF and time-dependent HF (TDHF) equations on a 3-D lattice. In 1995, Wells *et al*. [23] applied the basis-spline collocation method to the static and time-dependent Dirac equation which eliminated the "fermion doubling problem" that one encounters with the finite-difference method. In 1996, Kegley *et al*. [24] studied 2-D axially symmetric systems in cylindrical coordinates with the collocation method and also introduced the basis-spline Galerkin method. In the following, we compare both of these methods.

1. HFB lattice representation

For the lattice representation of wave functions and operators, we use a basis-spline method. Basis-spline functions $B_i^M(x)$ are piecewise-continuous polynomials of order $(M-1)$. They represent generalizations of finite elements which are basis splines with $M = 2$.

We consider an arbitrary (differential) operator equation,

$$\mathcal{O}\bar{f}(x) - \bar{g}(x) = 0. \tag{A1}$$

Special cases include eigenvalue equations of the HF/HFB type where the operator $\mathcal{O}$ represents the Hamiltonian and $\bar{g}(x) = E\bar{f}(x)$. We assume that both $\bar{f}(x)$ and $\bar{g}(x)$ are well approximated by spline functions

$$\begin{aligned} \bar{f}(x) &\approx f(x) \equiv \sum_{i=1}^{\mathcal{N}} B_i^M(x) a^i, \\ \bar{g}(x) &\approx g(x) \equiv \sum_{i=1}^{\mathcal{N}} B_i^M(x) b^i, \end{aligned} \tag{A2}$$

where a^i and b^i are expansion coefficients. Because the functions $f(x)$ and $g(x)$ are approximations to the exact functions $\bar{f}(x)$ and $\bar{g}(x)$, the operator equation will in general only be approximately fulfilled

$$\mathcal{O}f(x) - g(x) = R(x). \tag{A3}$$

The quantity $R(x)$ is called the *residual*; it is a measure of the accuracy of the lattice representation.

2. Basis-spline collocation method

In the collocation method, one minimizes the residual locally; i.e., one introduces a set of collocation (data) points x_α and requires that the residual vanish exactly at these points

$$R(x_\alpha) = 0. \tag{A4}$$

We multiply Eq. (A3) from the left with $\delta(x - x_\alpha)$ and integrate over x, including a volume element weight function $v(x)$ in the integrals to emphasize that the formalism applies to arbitrary curvilinear coordinates. Most cases of interest are covered by a function of the form

$$v(x) = x^p \quad p = \begin{cases} 0 & \text{Cartesian} \\ 1 & \text{polar} \\ 2 & \text{spherical.} \end{cases} \tag{A5}$$

Using the collocation condition Eq. (A4), one obtains

$$[\mathcal{O}f(x)]_{x_\alpha} - g(x_\alpha) = 0. \tag{A6}$$

Inserting the basis-spline expansion (A2) of the function $f(x)$ results in

$$\sum_i [\mathcal{O}B]_{\alpha i} a^i - g(x_\alpha) = 0, \tag{A7}$$

where we have introduced the short-hand notation

$$[\mathcal{O}B]_{\alpha i} = [\mathcal{O}B_i(x)]_{x_\alpha}. \tag{A8}$$

We eliminate the expansion coefficients a^i in Eq. (A7) by introducing the function values at the lattice support points x_α including both interior and boundary points

$$f_\alpha = f(x_\alpha) = \sum_i B_i(x_\alpha) a^i = \sum_i B_{\alpha i} a^i, \tag{A9}$$

$$g_\alpha = g(x_\alpha) = \sum_i B_i(x_\alpha) b^i = \sum_i B_{\alpha i} b^i. \tag{A10}$$

The matrix $B_{\alpha i}$ is, in general, rectangular. However, it can be made into a square matrix by adding either periodic or fixed boundary conditions; this is described in detail in Ref. [21,

23,24]. In what follows, the new (square) basis-spline matrix with the boundary conditions added is also denoted by $B_{\alpha i}$, for simplicity of notation. Because the matrix B is now a square matrix it can be inverted to eliminate the expansion coefficients a^i, b^i

$$a^i = \sum_\alpha B^{i\alpha} f_\alpha, \qquad b^i = \sum_\alpha B^{i\alpha} g_\alpha, \tag{A11}$$

resulting in

$$\sum_\beta \sum_i [\mathcal{O}B]_{\alpha i} B^{i\beta} f_\beta = g_\alpha. \tag{A12}$$

Defining the collocation lattice representation of the operator $\mathcal{O}$ via

$$\mathcal{O}_\alpha^\beta = \sum_i [\mathcal{O}B]_{\alpha i} B^{i\beta}, \tag{A13}$$

we arrive at the desired lattice representation

$$\sum_\beta \mathcal{O}_\alpha^\beta f_\beta = g_\alpha. \tag{A14}$$

3. Basis-spline Galerkin method

To derive the Galerkin representation, we multiply Eq. (A3) from the left with the spline function $B_k(x)$ and integrate over x

$$\int v(x)dx\, B_k(x)\mathcal{O}f(x) - \int v(x)dx\, B_k(x)g(x) = \int v(x)dx\, B_k(x)R(x). \tag{A15}$$

Various schemes exist to minimize the residual function $R(x)$; the Galerkin method requires that there be no overlap between the residual and an arbitrary basis-spline function

$$\int v(x)dx\, B_k(x)R(x) \stackrel{!}{=} 0. \tag{A16}$$

This so-called Galerkin condition amounts to a *global reduction of the residual*. We apply the Galerkin condition to Eq. (A15) and insert the basis-spline expansions for $f(x)$ and $g(x)$, Eq. (A2), resulting in

$$\sum_i \left[\int v(x)dx\, B_k(x)\mathcal{O}B_i(x)\right] a^i - \sum_i \left[\int v(x)dx\, B_k(x)B_i(x)\right] b^i = 0. \tag{A17}$$

Defining the matrix elements

$$\mathcal{O}_{ki} = \int v(x)dx\, B_k(x)\mathcal{O}B_i(x), \tag{A18}$$

$$G_{ki} = \int v(x)dx\, B_k(x)B_i(x), \tag{A19}$$

transforms the (differential) operator equation into a matrix $\times$ vector equation

$$\sum_i \mathcal{O}_{ki} a^i = \sum_i G_{ki} b^i, \tag{A20}$$

which can be implemented on modern vector or parallel computers with high efficiency. The matrix G_{ki} is sometimes referred to as the *Gram* matrix; it represents the nonvanishing overlap integrals between different basis-spline functions. This matrix possesses several highly desirable numerical properties; it is symmetric, banded, positive definite, and invertible for any reasonable placement of the knots and any spline order

$$\sum_k G^{jk} G_{ki} = \delta_i^j. \tag{A21}$$

We use again the relations (A11) to eliminate the expansion coefficients a^i and b^i in Eq. (A20), which results in the matrix equation on the Galerkin lattice

$$\sum_\beta \mathcal{O}_\alpha^\beta f_\beta = g_\alpha, \tag{A22}$$

with the differential operator definition on the Galerkin lattice

$$\mathcal{O}_\alpha^\beta = \sum_{ijk} B_{\alpha i} G^{ij} \mathcal{O}_{jk} B^{k\beta}. \tag{A23}$$

We are also extending our previous basis-spline work to include nonlinear grids. Use of a nonlinear lattice should be most useful for loosely bound systems near the proton or neutron drip lines. Non-Cartesian coordinates necessitate the use of fixed endpoint boundary conditions; much effort has been directed toward improving the treatment of these boundaries.

4. 2-D lattice representation of HFB wave functions and Hamiltonian

For a given angular momentum projection quantum number Ω, we solve the eigenvalue problem on a 2-D grid (r_α, z_β) where $\alpha = 1, \ldots, m$ and $\beta = 1, \ldots, n$.

The four components of the spinor wave function $\psi^{(4)}(r, z)$ are represented on the 2-D lattice by a product of basis-spline functions $B_i(x)$ evaluated at the lattice support points. For example, the spin-up component of the wave function ϕ_2 is represented in the form

$$\phi_2^\Omega(r_\alpha, z_\beta, \uparrow) = \sum_{i,j} B_i^M(r_\alpha) B_j^M(z_\beta) U_2^{ij}. \tag{A24}$$

Hence, the four-dimensional spinor wave function in coordinate space $\psi^{(4)}(r, z)$ becomes an array $\psi(N)$ of length $N = 4 \cdot m \cdot n$.

For the lattice representation of the HFB Hamiltonian, we use a hybrid method in which derivative operators are constructed using the Galerkin method; this amounts to a global error reduction. Local potentials are represented by the basis-spline collocation method (local error reduction).

The lattice representation transforms the differential operator equation into a matrix × vector equation

$$\sum_{\nu=1}^{N} \mathcal{H}_{\mu}^{\nu} \psi_{\nu}^{\Omega} = E_{\mu}^{\Omega} \psi_{\mu}^{\Omega} \quad (\mu = 1, \ldots, N). \tag{A25}$$

The 2-D HFB code is written in FORTRAN 95 and makes extensive use of new data concepts, dynamic memory allocation, and pointer variables.

5. 2-D basis-spline Poisson solver

In the current version of our HFB-2D-LATTICE code, we obtain the Coulomb potential U_c by solving the Poisson equation in cylindrical coordinates (ρ, z)

$$\frac{\partial^2 \phi(\rho, z)}{\partial \rho^2} + \frac{\phi(\rho, z)}{4\rho^2} + \frac{\partial^2 \phi(\rho, z)}{\partial z^2} = -4\pi e^2 \sqrt{\rho}\, \rho_p(\rho, z), \tag{A26}$$

where function ϕ is related to the Coulomb potential as $\phi = \sqrt{\rho} U_c$. The Poisson equation (A26) is solved under the following boundary conditions:

$$\phi(\rho \to 0, z) \to 0,$$

$$\phi(\rho, z \to \pm z_{\max}) \to \sqrt{\rho}\, U_c(\rho, \pm z_{\max}), \tag{A27}$$

$$\phi(\rho \to \rho_{\max}, z) \to \sqrt{\rho_{\max}} U_c(\rho_{\max}, z). \tag{A28}$$

In calculating the boundary conditions at large distances, we used the large distance expansion ($|\mathbf{r}| \gg |\mathbf{r}'|$) of the Coulomb potential U_c

$$U_c(\mathbf{r}) = e^2 \int \frac{\rho_p(\mathbf{r}')}{|\mathbf{r} - \mathbf{r}'|} d^3\mathbf{r}', \tag{A29}$$

$$\frac{1}{|\mathbf{r} - \mathbf{r}'|} = e^{-\mathbf{r}' \cdot \nabla} \frac{1}{|\mathbf{r}|} = \frac{1}{r} - \mathbf{r}' \cdot \nabla \frac{1}{r} + \frac{1}{2} (\mathbf{r}' \cdot \nabla)^2 \frac{1}{r} - \frac{1}{6} (\mathbf{r}' \cdot \nabla)^3 \frac{1}{r} + \frac{1}{24} (\mathbf{r}' \cdot \nabla)^4 \frac{1}{r} + \ldots, \tag{A30}$$

where we retained the terms up to the fourth order. The differential operators are represented on the lattice using the basis-spline Galerkin method.

[1] J. Dobaczewski, N. Michel, W. Nazarewicz, M. Ploszajczak, and M. V. Stoitsov, in *A New Era of Nuclear Structure Physics*, edited by Y. Suzuki, S. Ohya, M. Matsuo, and T. Ohtsubo (World Scientific, Singapore, 2004), pp. 162–171.

[2] J. Enders, H. Kaiser, P. von Neumann-Cosel, C. Rangacharyulu, and A. Richter, Phys. Rev. C **59**, R1851 (1999).

[3] E. Terán, V. E. Oberacker, and A. S. Umar, Phys. Rev. C **67**, 064314 (2003).

[4] V. E. Oberacker, A. S. Umar, E. Terán, and A. Blazkiewicz, Phys. Rev. C **68**, 064302 (2003).

[5] J. Dobaczewski, W. Nazarewicz, T. R. Werner, J. F. Berger, C. R. Chinn, and J. Dechargé, Phys. Rev. C **53**, 2809 (1996).

[6] V. E. Oberacker, A. S. Umar, A. Blazkiewicz, and E. Terán, in *A New Era of Nuclear Structure Physics*, edited by Y. Suzuki, S. Ohya, M. Matsuo, and T. Ohtsubo (World Scientific, Singapore, 2004), pp. 179–183.

[7] J. L. Egido, L. M. Robledo, and Y. Sun, Nucl. Phys. **A560**, 253 (1993).

[8] M. V. Stoitsov, J. Dobaczewski, W. Nazarewicz, S. Pittel, and D. J. Dean, Phys. Rev. C **68**, 054312 (2003).

[9] J. Terasaki, P. H. Heenen, H. Flocard, and P. Bonche, Nucl. Phys. **A600**, 371 (1996).

[10] M. Yamagami, K. Matsuyanagi, and M. Matsuo, Nucl. Phys. **A693**, 579 (2001).

[11] N. Tajima, Phys. Rev. C **69**, 034305 (2004).

[12] P. Campbell *et al.*, Phys. Rev. Lett. **89**, 082501 (2002).

[13] S. Rinta-Antila, S. Kopecky, V. S. Kolhinen, J. Hakala, J. Huikari, A. Jokinen, A. Nieminen, J. Äystö, and J. Szerypo, Phys. Rev. C **70**, 011301(R) (2004).

[14] E. Chabanat, P. Bonche, P. Haensel, J. Meyer, and R. Schaeffer, Nucl. Phys. **A635**, 231 (1998); **A643**, 441 (1998).

[15] M. V. Stoitsov, J. Dobaczewski, P. Ring, and S. Pittel, Phys. Rev. C **61**, 034311 (2000).

[16] *Half lives of isomeric states from SF of* ^{252}*Cf and large deformations in* ^{104}*Zr and* ^{158}*Sm*, J. K. Hwang, A. V. Ramayya, J. H. Hamilton, D. Fong, C. J. Beyer, P. M. Gore, E. F. Jones, E. Terán, V. E. Oberacker, A. S. Umar, Y. X. Luo, J. O. Rasmussen, S. J. Zhu, S. C. Wu, I. Y. Lee, P. Fallon, M. A. Stoyer, S. J. Asztalos, T. N. Ginter, J. D. Cole, G. M. Ter-Akopian, and R. Donangelo *et al.*, submitted to Phys. Rev. C (July 2003).

[17] G. Audi, A. H. Wapstra, and C. Thibault, Nucl. Phys. **A729**, 337 (2003).

[18] P. Möller, J. R. Nix, W. D. Myers, and W. J. Swiatecki, At. Data Nucl. Data Tables **59**, 185 (1995).

[19] G. A. Lalazissis, S. Raman, and P. Ring, At. Data Nucl. Data Tables **71**, 1 (1999).

[20] C. De Boor, *Practical Guide to Splines* (Springer Verlag, New York, 1978), and references therein.

[21] A. S. Umar, J. Wu, M. R. Strayer, and C. Bottcher, J. Comput. Phys. **93**, 426 (1991).

[22] A. S. Umar, M. R. Strayer, J.-S. Wu, D. J. Dean, and M. C. Güçlü, Phys. Rev. C **44**, 2512 (1991).

[23] J. C. Wells, V. E. Oberacker, M. R. Strayer, and A. S. Umar, Int. J. Mod. Phys. C **6**, 143 (1995).

[24] D. R. Kegley, V. E. Oberacker, M. R. Strayer, A. S. Umar, and J. C. Wells, J. Comput. Phys. **128**, 197 (1996).